ACS Appl. Mater. Interfaces **2019**, *11*, 23692-23700
https://doi.org/10.1021/acsami.9b04875

Sensing Nitrogen Mustard Gas Simulant at the ppb-Scale *via* Selective Dual-Site Activation at Au/Mn_3O_4 Interfaces

Lorenzo Bigiani,[†] Dario Zappa,[‡] Davide Barreca,*[,§] Alberto Gasparotto,[†] Cinzia Sada,[||] Gloria Tabacchi,[⊥] Ettore Fois,[⊥] Elisabetta Comini,[‡] and Chiara Maccato*[,†]

[†] Department of Chemical Sciences, Padova University and INSTM, Via Marzolo 1, 35131 Padova, Italy

[‡] Sensor Lab, Department of Information Engineering, Brescia University, Via Valotti 9, 25133 Brescia, Italy

[§] CNR-ICMATE and INSTM, Department of Chemical Sciences, Padova University, Via Marzolo 1, 35131 Padova, Italy

[||] Department of Physics and Astronomy, Padova University and INSTM, Via Marzolo 8, 35131 Padova, Italy

[⊥] Department of Science and High Technology, Insubria University and INSTM, Via Valleggio 11, 22100 Como, Italy

ABSTRACT: The efficient detection of chemical warfare agents (CWAs), putting at stake human life and global safety, is of paramount importance in the development of reliable sensing devices for safety applications. Herein, we present the fabrication of Mn_3O_4-based nanocomposites containing noble metal particles for the gas phase detection of a simulant of vescicant nitrogen mustard, *i.e.* di(propyleneglycol) monomethyl ether (DPGME). The target materials were fabricated by chemical vapor deposition of manganese oxide on Al_2O_3 substrates and subsequent functionalization with silver or gold *via* radio frequency sputtering. The obtained high purity composites, characterized by an intimate metal/oxide contact, yielded an outstanding efficiency in the detection of DPGME. In particular, sensing of the latter analyte with an ultra-low detection limit of 0.6 ppb could be performed selectively with respect to other CWA simulants. In addition, the tuneability of selectivity patterns as a function of metal nanoparticle nature paves the way to the development of efficient and selective devices for practical end-uses.

KEYWORDS: Mn_3O_4, Au, Ag, nanosystems, gas sensors, di(propyleneglycol) monomethyl ether

■ INTRODUCTION

The increased threats of chemical attacks by terrorist organizations have stimulated a significant interest in the early detection of chemical warfare agents (CWAs),[1-5] which is imperative for security reasons.[6-9] Since CWAs are extremely toxic[10] and require special infrastructures for storage/manipulation,[1] the activities aimed at their detection are carried out on mimicking compounds compatible with lab test security level.[6,8-9] In this context, the identification of di(propyleneglycol) monomethyl ether (DPGME), simulant of the vescicant nitrogen mustard,[2-3,11-12] is of key importance for safety applications.

Among the various methods and devices adopted up to date for CWA sensing,[4,6-7,9,13] chemoresistive gas sensors based on nanostructured metal oxides offer various advantages, encompassing low cost, limited power consumption and good stability/sensitivity.[3,7,14-21] Up to date, DPGME detection has been performed only in a few cases by the use of SnO_2-based systems,[2-5,12,22] and the development of highly efficient sensors for its selective monitoring is of paramount importance for next generation devices.

Among metal oxides, *p*-type Mn_3O_4, a mixed-valence, environmentally friendly and low-cost multi-functional system,[14,23-24] has been used so far for the detection of different analytes, thanks to the tunable Mn redox chemistry and its inherent catalytic properties.[18-20,25-26] However, gas sensors based on pure Mn_3O_4 typically feature responses lower than *n*-type systems,[16] as well as modest sensitivity/selectivity.[27-29] A valuable approach to circumvent these drawbacks is represented by the development of Mn_3O_4-based composites containing noble metals particles, like Ag and Au. The latter can in fact act as catalytic promoters of the involved chemical reactions at the nanoscale[30-34] and/or favor the formation of metal/oxide Schottky junctions, improving charge carrier separation.[14,35-36] Nevertheless, only one previous report on Mn_3O_4-Ag gas sensors is available in the literature up to date,[14] whereas, to the best of our knowledge, no studies on the functional performances of Mn_3O_4-Au sensors have ever been documented so far. In this regard, versatile routes to the target nanomaterials with controllable properties are highly demanded, and represent a strategic

ACS Appl. Mater. Interfaces **2019**, *11*, 23692-23700
https://doi.org/10.1021/acsami.9b04875

subject of ongoing investigation.[26,28]

Basing on preliminary results on the development of pure Mn_3O_4 nanomaterials as gas sensors,[26,37] in the present study we report for the first time on the gas sensing performances of nanocomposite systems based on Mn_3O_4-Ag and Mn_3O_4-Au in DPGME detection. The target materials were obtained by the initial chemical vapor deposition (CVD) of Mn_3O_4 on polycrystalline Al_2O_3 substrates, followed by silver or gold radio frequency (RF)-sputtering

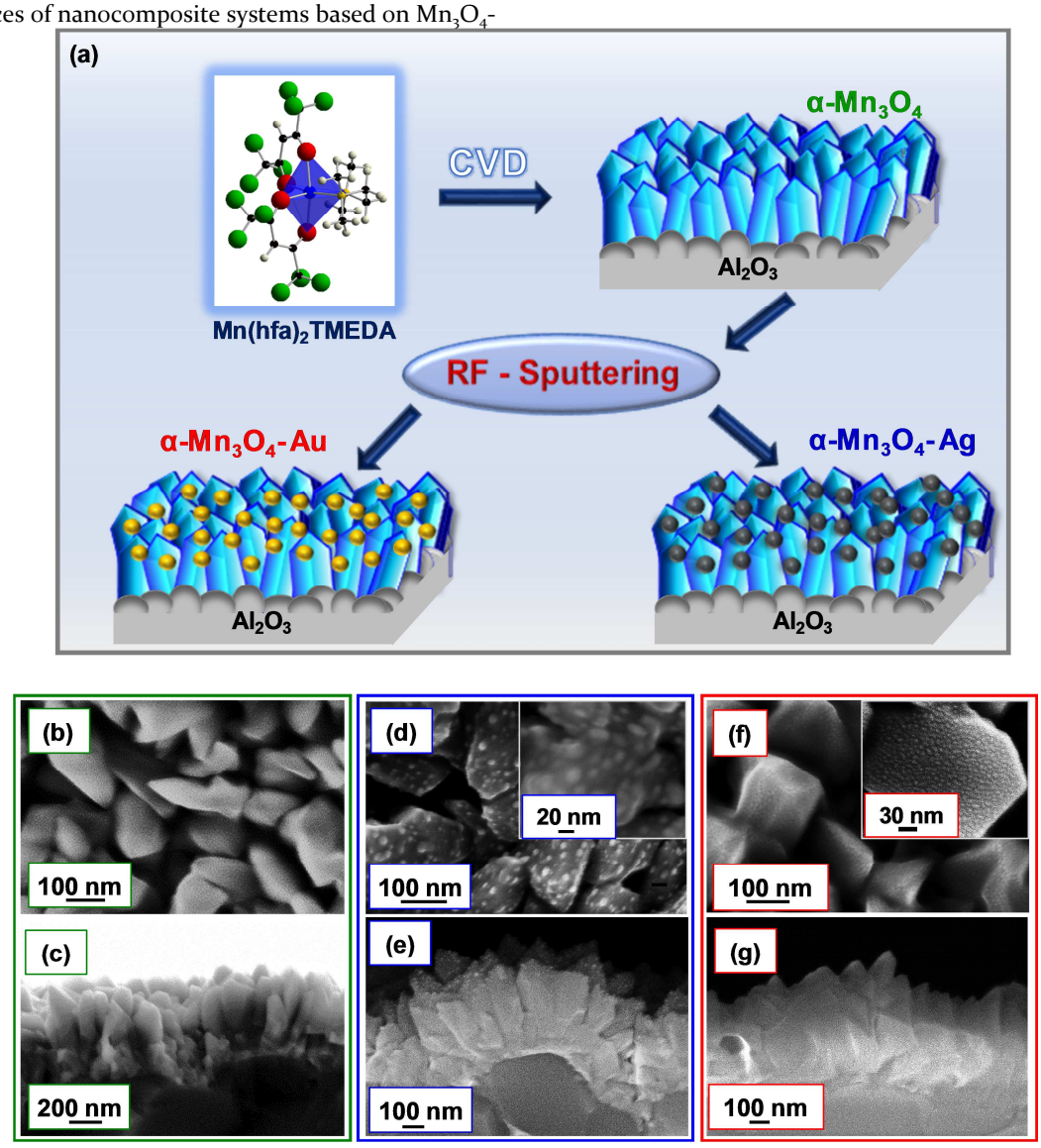

Figure 1. (a) Sketch of the synthetic approach used for the preparation of Mn_3O_4 nanosystems and their functionalization with Ag or Au NPs. Plane-view and cross-sectional FE-SEM micrographs for Mn_3O_4 (b,c), Mn_3O_4-Ag (d,e) and Mn_3O_4-Au (f,g) nanocomposites. The insets in (d) and (f) show Ag and Au NPs decorating the underlying Mn_3O_4.

under mild conditions (Figure 1a). In particular, we demonstrate the impact of Mn_3O_4 functionalization with Ag or Au nanoparticles (NPs) in obtaining an ultrasensitive DPGME detection. Moreover, the possibility of discriminating between DPGME, on one side, and acetonitrile (CH_3CN) or dimethyl methyl phosphonate (DMMP), simulants of HCN (blood agent gas) and Sarin nerve gas, respectively,[2,4,7-9,37] demonstrates the system selectivity towards the target warfare gas simulant. The system performances are also validated as a function of metal NP nature in the comparative sensing of acetone and ethanol, whose detection is of interest for various applications.[18-19,38-39] Beyond a systematic experimental characterization, density functional theory (DFT)-based calculations, per-

formed for the first time on the target nanocomposites, provide a molecular insight into the interactions between the target systems and DPGME. The results enabled to elucidate a dual-site activation mechanism based on the binding of DPGME to both manganese oxide and gold nanoparticles.

■ EXPERIMENTAL SECTION

Synthesis. Fabrication of the sensing materials was carried out on polycrystalline Al_2O_3 substrates (Maruwa, purity = 99.6%; lateral dimensions = 3 mm × 3 mm, thickness = 0.25 mm), subjected to a cleaning procedure prior to each deposition.[37] Basing on previously obtained results,[26,37] CVD of Mn_3O_4 was carried out for 60 min at a growth temperature of 500°C and a total pressure of 10.0 mbar. These conditions corresponded to the obtainment of supported nanosystems endowed with a high porosity. Functionalization of the pristine Mn_3O_4 systems with Ag or Au was carried out by RF-sputtering at a temperature of 60°C and a pressure of 0.3 mbar. The deposition time was set at 45 min for Ag and 30 min for Au, to obtain a comparable metal loading in the resulting nanocomposites. These processing parameters were identified after a careful preliminary screening of preparative conditions**.** This led us to discard the use of higher RF-powers or longer deposition times to prevent alterations of the underlying Mn_3O_4 and avoid the obtainment of a too high metal NP surface density, leading ultimately to their coalescence and to the formation of continuous films with reduced porosity. All the obtained Mn_3O_4-based composite systems were analyzed as-prepared, avoiding any *ex-situ* annealing in order to prevent the conversion of Mn_3O_4 into other Mn oxides.[40] Further details are reported in the Supporting Information.

Characterization. Field emission-scanning electron microscopy (FE-SEM) and energy dispersive X-ray spectroscopy (EDXS) analyses were performed by a Zeiss SUPRA 40 VP instrument equipped with an Oxford INCA x-sight X-ray detector, using primary beam voltages between 10 and 20 kV.

X-ray diffraction (XRD) patterns were recorded at an incidence angle of 1.0° by a Bruker D8 Advance diffractometer equipped with a Göbel mirror and a Cu Kα X-ray source operated at 40 kV and 40 mA. The average crystallite size was estimated by the Scherrer equation.[18-19]

X-ray photoelectron spectroscopy (XPS) analyses were performed on a Perkin-Elmer Φ 5600-ci spectrometer using a non-monochromatic Al Kα radiation (1486.6 eV), at pressures lower than 10^{-8} mbar. No sign of sample degradation was observed due to X-ray irradiation. The measured binding energy (BE) values (standard deviation = ± 0.2 eV) were corrected for charging effects by assigning to the C1s peak, associated with adventitious hydrocarbons, a value of 284.8 eV.[41]

Secondary ion mass spectrometry (SIMS) measurements were carried out by means of an IMS 4f mass spectrometer using a Cs^+ primary ion beam (14.5 keV, 25 nA) and by negative secondary ion detection. Charge compensation was achieved by means of an electron gun. In the abscissa of each plot, the sputtering time was converted into depth using the deposit thickness values measured by cross-sectional FE-SEM measurements.

Gas sensing tests. Conductometric devices were fabricated by depositing Pt interdigited electrodes (IDEs) on top of the Mn_3O_4 layer and a Pt heating element on the backside of the alumina substrates (Figure S1). Gas sensing tests were performed in a sealed climatic chamber (20°C; relative humidity level = 40%, in order to simulate real ambient conditions). A constant synthetic air flow (rate = 300 SCCM) at atmospheric pressure was used as a carrier gas, and the atmosphere composition was controlled using mass flow controllers (MKS, Germany) to mix flows coming from certified gas bottles (SIAD, Italy) containing a precise concentration of target analytes diluted in synthetic air. The output signal was measured by applying a constant bias of 1 V to the sensing materials and measuring the resulting current by means of a picoammeter (Keithley, USA). The target sensors did not show any appreciable short-term drifts in the baseline resistance over a time period up to 12 h. The reproducibility and repeatability of the devices was investigated by performing measurements on up to 8 identical sensors under the same experimental conditions, yielding an estimated maximum uncertainty of ± 10%. The same variation was also estimated as the response drift over two months of tests, demonstrating thus an appreciable stability, an important starting point in view of eventual practical applications.[28] The lifetime of the present Mn_3O_4 sensors can be estimated to be > 1 year, over which the samples are still working without any evident deterioration.

The IDLH (immediately dangerous for life and health) value[17] and median lethal dose are defined as the threshold concentration producing permanent health problems for exposure times > 30 min,[37] and the dose required to kill half the members of a tested population,[1,6-7] respectively.

Computational details. Electron-electron interaction was accounted by the PBE approximation,[42] augmented *via* the Grimme D2 correction for dispersion.[43] Mn atoms were treated using the Hubbard model,[44] adopting an U parameter of 5 eV.[24] Ultrasoft pseudopotentials[45] were adopted for all atoms, the planewave basis set was truncated at 30 Ry (240 Ry for the electron density), and a 2 × 2 × 1 mesh was adopted for the Brillouin zone sampling. Calculations were performed with the Quantum Espresso Code.[46]

Additional details on chemico-physical and functional characterization, as well as further computational details, can be found in the Supporting information.

■ RESULTS AND DISCUSSION

The morphology of the target materials was investigated by FE-SEM. In line with previous results,[26,31] bare Mn_3O_4 (Figure 1b) was characterized by an even distribution of faceted nanoaggregates with a mean size of (110 nm × 270 nm), whose assembly yielded the formation of porous arrays[26] [deposit thickness = (510 ± 30) nm, Figure 1c]. Upon RF-sputtering of silver (Figures 1d and 1e) and gold (Fig-

ures 1f and 1g), the pristine Mn_3O_4 morphology and thickness did not undergo remarkable alterations, as also demonstrated by atomic force microscopy (AFM) analyses (Figure S2). Nevertheless, a careful inspection of higher resolution FE-SEM micrographs (insets of Figures 1d and f) enabled to discern the presence of low-sized nanoparticles (∅ ≈ 10 and 6 nm for Ag and Au, respectively, homogeneously dispersed over the surface of Mn_3O_4 grains. EDXS line-scans (Figure S3) evidenced similar profiles for Mn and O X-ray signals, confirming the nanodeposits compositional homogeneity, and revealed that Ag and Au were present even in the Mn_3O_4 inner regions. These results were further corroborated by SIMS (see below).

The system microstructure was investigated by XRD analyses. Beside reflections due to the alumina substrate, the recorded patterns (Figure S4) revealed the presence of diffraction peaks at 2θ = 18.0°, 28.9°, 31.0°, 32.3°, 36.1°, 37.9°, and 44.5°. These signals were indexed respectively to the (101), (112), (200), (103), (211), (004) and (220) crystallographic planes of tetragonal α-Mn_3O_4 (*hausmannite*;[47] space group $I4_1/amd$; a = 5.762 Å, c = 9.470 Å; average crystallite size ≈40 nm). Neither additional diffraction peaks from other Mn-containing oxides, nor significant peak shift with respect to the powder reference pattern were observed. Nevertheless, the relative intensity of (211) signals was higher for the present samples, suggesting a preferential exposure of (211) planes.[26,37] No appreciable variation of XRD patterns took place after Ag or Au introduction, a phenomenon due to the use of mild RF-sputtering conditions, which yielded a high dispersion and a relatively low loading of Ag and Au NPs (see FE-SEM and XPS results).[33,35-36] This finding highlights that the proposed functionalization strategy is mild enough to maintain unaltered the original oxide structure.

XPS wide-scan spectra (Figure S5a) revealed the presence of Mn, O and, eventually, of Ag/Au, along with a C contribution resulting from atmospheric exposure. Irrespective of the preparative conditions, the results unambiguously confirmed the formation of Mn_3O_4 as the sole manganese oxide (BE($Mn2p_{3/2}$) = 641.9 eV, Figure 2a;[15,26,29-30,32] multiplet splitting separation of Mn3s components = 5.4 eV,[31] Figure S5b; BE difference between $Mn2p_{3/2}$ and O1s lattice components = 112.0 eV,[20,30]). After functionalization, the analysis yielded similar values for Ag and Au surface molar fractions (X_{Ag} = 53.0%; X_{Ag} = 58.0%). As regards Ag-containing systems [BE($Ag3d_{5/2}$) = 368.6 eV, Figure 2b], calculation of silver Auger parameters (see the Supporting Information; α_1 = 719.6 eV, α_2 = 725.6 eV) evidenced the co-existence of Ag(0) and Ag(I) oxide, highlighting a partial Ag(0) → Ag(I) surface oxidation. This phenomenon, typically encountered in the case of silver nanoparticles deposited by sputtering on various metal oxide systems,[33-34,36] can be traced back to their high reactivity with both air from the surrounding atmosphere and the supporting Mn_3O_4 systems. In a different way, gold, less reactive towards oxidation, was present in its pure metallic state [BE($Au4f_{7/2}$) = 84.4 eV, SOS = 3.6 eV; BE ($Au4d_{5/2}$) = 335.4 eV; see Figures 2c and S5c]. The slightly higher BE values (≈0.5 eV) with respect to the typical ones reported for metallic Au[32,35,48-50] evidenced the formation of Schottky junctions at the Au/Mn_3O_4 interface.[33] In particular, the intimate metal/oxide contact is likely to result in an electron flow from gold to the empty states of Mn_3O_4 valence band, producing a gold charge density decrease and a corresponding upward BE shift of Au peaks. As shown below, these phenomena have a remarkable influence on the gas sensing performances of Mn_3O_4-Au systems.

For all samples, the surface O1s peak could be deconvoluted by means of two distinct components (Figure S6) The low BE one (**I**, BE = 529.9 eV; typically 72% of the total oxygen for Mn_3O_4 and Mn_3O_4-Au sample, and 56% for Mn_3O_4-Ag specimen) was ascribed to lattice oxygen in Mn_3O_4[32,51-53] and, for Mn_3O_4-Ag, resulted even from the contribution of Ag(I) oxide.[51,54] The second band (II), located at BE = 531.5 eV (28% of the total oxygen signal for Mn_3O_4 and Mn_3O_4-Au sample, and 44% for Mn_3O_4-Ag specimen) was attributed to the contribution of surface-adsorbed oxygen species.[21,36,54-58] The presence of the latter, directly involved in the gas sensing process and exerting a beneficial influence on gas sensing performances,[26] results in a O/Mn atomic ratio close to 1.5, slightly higher than the value expected for stoichiometric Mn_3O_4.

To investigate the in-depth chemical composition, SIMS analyses were carried out (Figures 2d and e). In general, C presence (signal not displayed) was limited to the outermost 10 nm, indicating the purity of the target nanomaterials. The parallel Mn and O ionic yields throughout the whole deposits depth indicated an homogeneous composition, and the relatively broad interface with the Al_2O_3 substrates was traced back to the inherent roughness of the latter.[26] As can be noted, a higher metal concentration in a near-surface region of ≈100 nm was obtained, and both Ag and Au signals underwent a progressive decrease at higher

ACS Appl. Mater. Interfaces **2019**, *11*, 23692-23700
https://doi.org/10.1021/acsami.9b04875

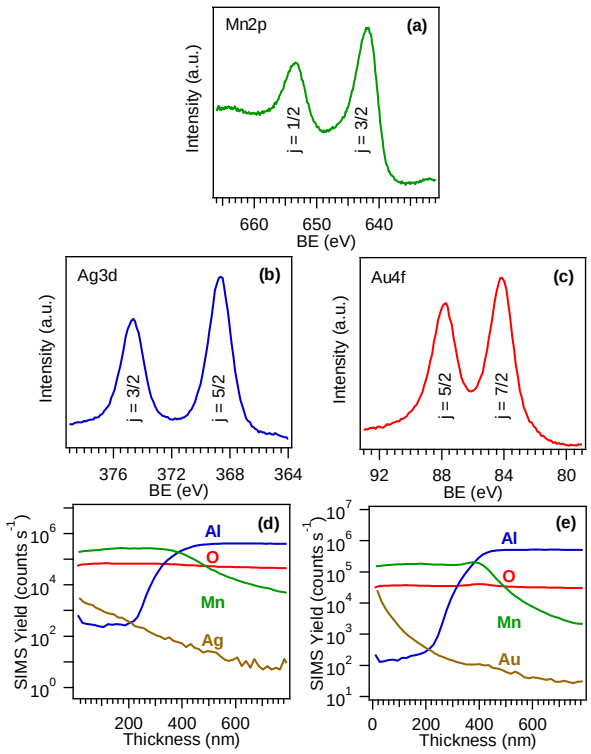

Figure 2. (a) Mn2p, (b) Ag3d and (c) Au4f peaks for the analyzed specimens. Color codes: Mn_3O_4, green; Mn_3O_4-Ag, blue; Mn_3O_4-Au, red. SIMS depth profiles for (d) Mn_3O_4-Ag and (e) Mn_3O_4-Au samples.

depths. In both cases, the in-depth intimate Ag(Au)/Mn_3O_4 contact was traced back to the synergy between the oxide nanodeposit porosity and the inherent RF-sputtering infiltration power.

The sensing responses of bare and functionalized Mn_3O_4 systems were preliminarily screened towards acetone and ethanol, whose detection is less challenging than DPGME. The obtained dynamic response curves (Figures 3a and 3b) revealed a conductance drop-off upon gas exposure, as expected in the case of *p*-type Mn_3O_4, due to a decrease of majority carrier density upon analyte reaction with adsorbed oxygen species.[25-27] The observed variations were proportional to the concentration of both gases, without any significant saturation, at variance with previous Mn_3O_4-based sensors.[15,28] Concomitantly, the good air state recovery at the end of gas pulses confirmed a reversible analyte-sensor interaction.[25-26,35] These issues were corroborated by the linear response *vs.* concentration trends (Figures 3c and 3d, Table S1).

The observed response order (Mn_3O_4 < Mn_3O_4-Ag < Mn_3O_4-Au), highlighting the beneficial influence of Mn_3O_4-Ag and Mn_3O_4-Au interactions on the sensing behavior,[14] could be explained taking into account that the system performances were directly affected by both the nature and chemical state of the introduced metal NPs.[33,36] In particular, the gas sensing mechanism accepted for *p*-type oxide chemoresistors like Mn_3O_4 involves the initial O_2 chemisorption yielding active oxygen species, among which O^- ions are the predominant ones in the adopted temperature interval.[37,58] This results in the formation of a

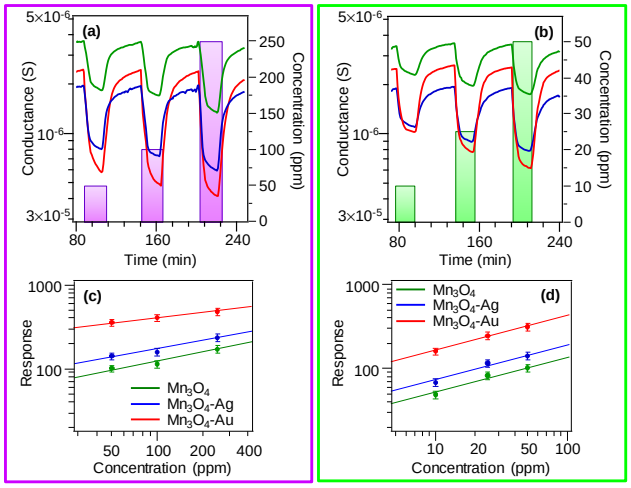

Figure 3. Dynamic responses to acetone (a) and ethanol (b) for Mn_3O_4, Mn_3O_4-Ag and Mn_3O_4-Au specimens. Responses of the same samples *vs.* acetone (c) and ethanol (d) concentrations. The data were obtained at 300°C, the optimal working temperature for the detection of these analytes, regardless of the system chemical composition.

near-surface hole accumulation layer (HAL),[16,27-28] whose width decreases upon chemisorption of reducing analytes (like the present ones), due to electron release into the system conduction band[26] (see also reactions (S3)-(S5) in the Supporting Information section). This phenomenon accounts for the conductance drop observed upon gas exposure, an effect which is overturned upon restoring the original air situation.[15] Which is the influence of the introduced noble metals in this regard? In principle, metal NPs can catalyze the chemical reactions involved in the sensing process and/or act as electronic sensitizers.[14] The latter effect, likely to be the predominant one in the present case, is significantly enhanced by the above discussed Ag(Au)/Mn_3O_4 contact.[36] In particular, the formation of Au/Mn_3O_4 Schottky junctions,[35] resulting in an Au→Mn_3O_4 electron flow (see the above XPS data), is responsible of higher HAL modulations upon analyte interaction with respect to bare Mn_3O_4.[29] Differently from Au, Ag yields a lower efficiency in promoting the sensing process due to its partial surface oxidation (see above), preventing the effective establishment of Ag/Mn_3O_4 Schottky junc-

tions.[33]

Notably, the best response values towards acetone and ethanol for Ag and, in particular, Au-containing systems were higher not only than those of *p*- and *n*-type oxide nanosystems containing metal NPs (such as CuO- TiO_2-Au[35] and Fe_2O_3-Ag[36]), but also than all those reported so far for Mn_3O_4-containing sensors under analogous working conditions.[14-15,18-19,25,27-29] The estimated detection limits decreased from bare Mn_3O_4 (10 ppb, acetone; 1.0 ppm, ethanol)[26] to Mn_3O_4-Ag and, finally, Mn_3O_4-Au (1.5 ppb, acetone; 0.4 ppm; ethanol). The best values obtained for the latter systems were significantly lower than the threshold used for screening ethanol in an intoxicated driver (200 ppm),[29] inferior to those of various oxide systems[35-36] and favorably compared with those reported for chemoresistors based on Mn_3O_4.[25]

The attention was subsequently focused on CWA detection, with particular regard to DPGME sensing, the main focus of the present investigation. Since the sensor selectivity is a key concern for practical applications,[15,20] efforts were also dedicated to testing other CWA simulants, namely acetonitrile and DMMP, as potential interferents yielding false alarms. In this regard, Figure 4a reports a general overview of response values to selected acetonitrile, DMMP and DPGME concentrations as a function of the operating temperature, a critical factor in determining sensor performances.[15,26] The results show that, whereas bare Mn_3O_4 yields relatively low responses to the various analytes for temperatures ≤ 250°C, a more pronounced detection efficiency towards DPGME could be obtained at 300°C. The latter trend, indicating an enhanced reaction between the analyte and adsorbed oxygen upon increasing the thermal energy supply, was maintained even upon Mn_3O_4 functionalization with Ag, although the DPGME responses underwent a systematic increase, which was nearly two-fold at 300°C. In a different way, for the Mn_3O_4-Au sensor, the maximum DPGME response, outperforming all the other ones, was registered at an operating temperature of 200°C and underwent a progressive decrease at higher working temperature, as previously reported for DPGME sensing.[1,3-5] This phenomenon suggested that, for higher temperatures, the decreased analyte adsorption, resulting in a less efficient interaction with the active material, was not sufficiently compensated by the increased extent of surface reactions.[37] In particular, the downward shift of the optimal working temperature confirmed the valuable sensitization exerted by Au nanoparticles.[35] Such a result empowers the efficient and selective DPGME detection already at 200°C, a temperature lower than those previously utilized,[2,4] decreasing the power consumption and broadening the scenario of possible technological applications. Taken together, the obtained data reveal that the functionalization of bare Mn_3O_4 with Ag or Au NPs is a proficient mean to produce not only a significant increase of the sensor response to DPGME, but also a remarkable selectivity towards this analyte with respect to other CWA simulants, namely acetonitrile and DMMP. In fact, a careful inspection of Figure 4a evidences that, for each temperature, acetonitrile and DMMP responses were suppressed by the introduction of Ag and Au NPs in the pristine Mn_3O_4 system, whereas the responses to DPGME were significantly boosted, especially for gold-containing sensors. Figure 4b shows that the DPGME response was significantly higher than those of the other gases, candidating Au-Mn_3O_4 sensors as optimal candidates for the selective monitoring of this simulant. These results have significant implications, taking into account that they do not require complex systems/methods, like electronic noses/sensor arrays/data processing,[4,14] and that previous Mn_3O_4 sensors showed no significant selectivity.[29]

Notably, the best response values to DPGME displayed by the present Mn_3O_4-Au nanomaterials are the highest ever reported in the literature for DPGME detection by chemoresistive SnO_2-containing gas sensors,[2-3,12]

ACS Appl. Mater. Interfaces **2019**, *11*, 23692-23700
https://doi.org/10.1021/acsami.9b04875

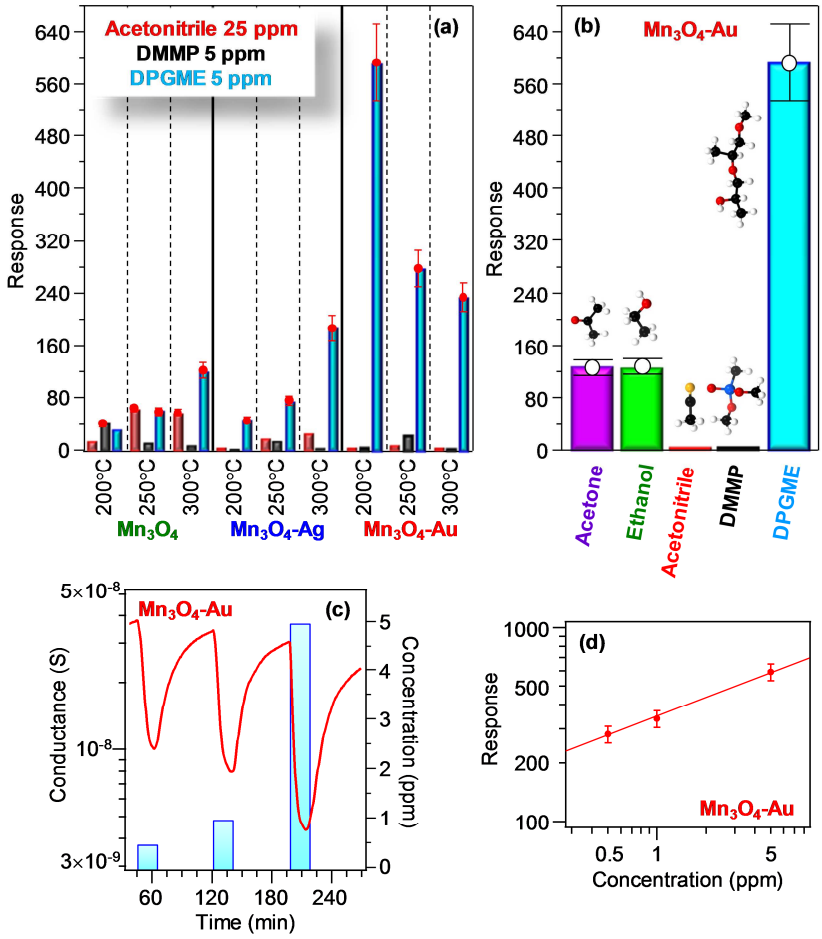

Figure 4. (a) Responses of Mn_3O_4, Mn_3O_4-Ag and Mn_3O_4-Au sensors to selected concentrations of various CWAs at different operating temperatures. (b) Responses at 200°C of Mn_3O_4-Au to various analytes (acetone, 100 ppm; ethanol, 50 ppm; acetonitrile, 25 ppm; DMMP, 5 ppm; DPGME, 5 ppm). Dynamic response to DPGME (c) and response *vs*. DPGME concentration (d) for Mn_3O_4-Au at 200°C.

and even the actual bare Mn_3O_4 outperforms some of the previously reported tin dioxide-based systems.[4-5] These very attractive functional performances could be related to the morphological organization of the target materials and, in particular, to their inherent porosity, with voids extending into the system structure, ensuring a high contact area for the interaction with gaseous analytes.[15,18] A predominant key contribution for metal NP-containing sensors arises from the intimate contact between Mn_3O_4 and the introduced metal particles, producing a good intergranular coupling, an important issue for the successful exploitation of mutual electronic interplay.[27,33,35-36] In particular, as previously discussed, whereas the partial Ag surface oxidation hinders the effective formation of Ag/Mn_3O_4 Schottky junctions, the occurrence of the latter, taking place in Au/Mn_3O_4 sensors, is responsible for the significantly higher gas response, especially at 200°C. In addition, the sensitization effects exerted by noble gold NPs is also responsible for the remarkable selectivity towards DPGME of Mn_3O_4-Au sensors. Nevertheless, only a limited number of works have been focused on these topics, and additional investigation is undoubtedly needed to unravel the related effects,[27] since the sensor selectivity is influenced in a complex way by the sensing material morphology and surface active sites.[2,26]

Dynamic response curves of the target sensors upon exposure to DPGME concentration pulses at the optimal working temperature for each system (Figures S7 and 4c) confirmed that the sensor efficiency increased according to the previously reported order, *i.e.* Mn_3O_4 < Mn_3O_4-Ag < Mn_3O_4-Au. In line with the above mentioned *p*-type behavior (see above),[25-26] a conductance drop-off took place upon contact with the target analyte. The rapid signal decrease, followed by a slower variation up to the end of the

ACS Appl. Mater. Interfaces **2019**, *11*, 23692-23700
https://doi.org/10.1021/acsami.9b04875

pulse, as observed in the case of SnO_2 sensors,[5] indicated that DPGME molecular adsorption was the rate-limiting step of the overall process.[37] The response dynamics also showed a sluggish conductance reversal to the initial state when air contact was restored, leading to an incomplete baseline recovery. This behavior, that was progressively more marked at increasing analyte concentrations, was attributed to the slow analyte desorption and suggested the possible

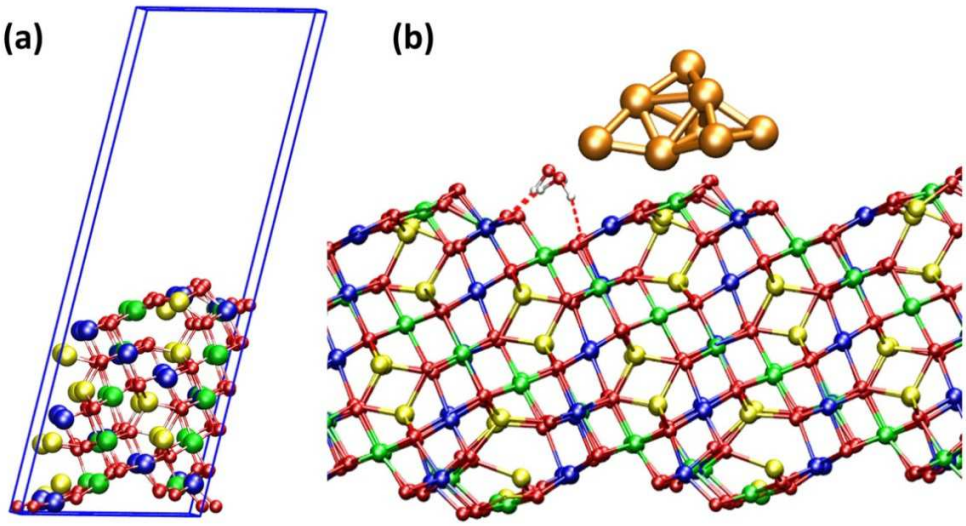

Figure 5. (a) Graphical representation of the optimized structure of bare *hausmannite* (211) slab. Color codes: red, oxygen; yellow, tetrahedral Mn^{2+}; blue (up-spin) and green (down-spin), octahedral Mn^{3+}. The blue lines represent the periodic cell adopted in all calculations (cell parameters: a = 11.085 Å, b = 12.493 Å, c = 30 Å; α = 95.21°, β = 75.63°, γ = 114.07°). (b) Graphical representation of the active-slab model (orange: Au, white: H). Hydrogen bonds are sketched as dashed red lines.

occurrence of a progressive chemical poisoning of the sensor surface,[2,5,17,37] an issue which is usually reduced at high working temperatures and that has to be properly considered for further implementation. In this case, however, the poisoning effect is very low, slowing down the recovery rate of the devices but without leading to irreversible surface changes.

In spite of these phenomena, the dependence of the sensor responses on DPGME concentration in the log-log scale (Figures 4d and S8) indicated an increase proportional to DPGME concentration for all the analyzed systems. At variance with previous reports on DPGME detection by SnO_2 sensors,[2,5] this linear behavior excluded appreciable saturation phenomena,[35,37] an important prerequisite for eventual end-uses. The detection limits extrapolated from these curves underwent a progressive lowering from pure Mn_3O_4

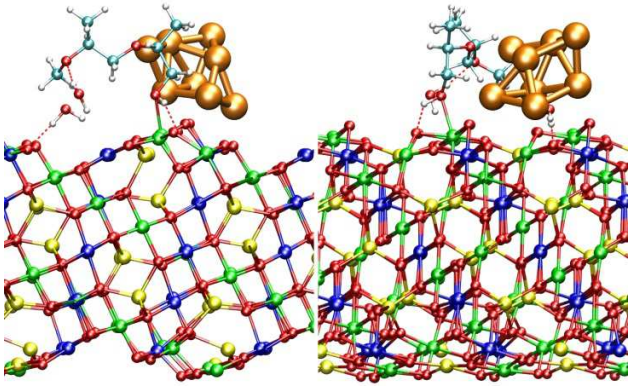

Figure 6. Graphical representations of the geometry-optimized DPGME + active-slab model in different orientations. Color codes: red, oxygen, yellow, tetrahedral Mn^{2+}; blue (up-spin) and green (down-spin), octahedral Mn^{3+}; orange, Au; cyan, C; white, H. Hydrogen bonds are sketched as dashed red lines.

(50 ppb) to Mn_3O_4-Au (0.6 ppb). Notably, these values, and, in particular, the latter one, were much lower than the ones previously obtained by love-wave sensors.[8-9] In addition, the obtained limits were six orders of magnitude below the reported DPGME immediately dangerous for

ACS Appl. Mater. Interfaces **2019**, *11*, 23692-23700
https://doi.org/10.1021/acsami.9b04875

life and health (IDLH) value and median lethal dose.[1,6-7,17,59] These results pave the way to an eventual ultra-sensitive DPGME detection by sensor devices for safety application.

In order to attain a deeper insight into gas molecule interactions with Mn_3O_4-based nanocomposite systems and improve our understanding of the interactions occurring at atomistic level, DFT calculations were performed, by creating a slab model of Mn_3O_4 (211) surfaces, which, on the basis of XRD results (see above), are the ones preferentially exposed. In particular, the attention was focused on the best performing sensor, Mn_3O_4-Au, towards the detection of DPGME and ethanol. The (211) Mn_3O_4 surface (Figure 5) was simulated by cutting a periodic slab model from a Mn_3O_4 crystalline structure adopting previously reported *hausmannite* cell parameters.[47] Herein, we mostly focus on structural results of the active-slab + DPGME model system (Figures 6 and 7) in order to highlight the main interactions responsible for the observed behavior (see Supporting information for the Mn_3O_4-Au/ethanol system).

The key findings of theoretical investigation can be summarized as follows: i) on the active surface, the Au cluster interacts with the Mn_3O_4 oxygen anions (three Au–O_{Mn} short distances, *i.e.* 2.10 Å, 2.13 Å and 2.24 Å), thus supporting at the atomic scale level the occurrence of an intimate Au/Mn_3O_4 contact (see above); ii) both Mn_3O_4 and Au NP surfaces are directly involved in the interaction with DPGME (see Figure 6), revealing a dual-site contact. Indeed, the hydroxyl DPGME oxygen is found at a very close distance (2.18 Å) from a surface Mn^{3+} (which therefore recovers its full octahedral coordination), whereas an ethereal DPGME oxygen lies at 2.35 Å from a gold atom.

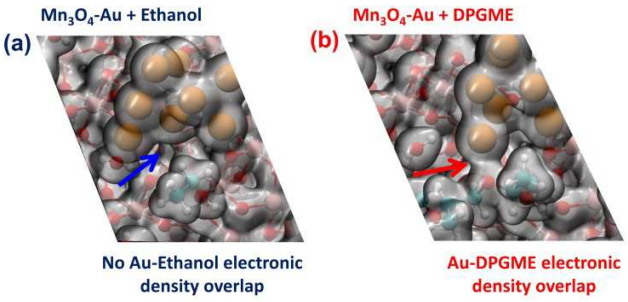

Figure 7. Graphical representations (top view) of the geometry-optimized (a) Mn_3O_4-Au-ethanol model and (b) Mn_3O_4-Au-DPGME model showing, as grey shaded envelope, the electronic density (isovalue = 0.02 electrons $Å^{-3}$). Color codes: red, oxygen; pink, Mn^{2+}/Mn^{3+}; orange, Au; cyan; C; white, H.

The presence of the DPGME molecule slightly perturbs the shortest Au-surface contacts (2.11 Å, 2.22 Å and 2.24 Å, for the three distances reported above respectively). Moreover, DPGME is also involved in strong hydrogen bonds: its hydroxyl proton is at 1.68 Å from a surface oxygen, whereas a surface water proton is at 1.86 Å from the second ethereal oxygen. A comparison with the Mn_3O_4-Au-ethanol system reveals that also ethanol is coordinated to a surface Mn^{3+} cation located close to the Au cluster (Figure S9). The distance of the hydroxyl oxygen from Mn^{3+}, 2.09 Å, is shorter than that found for DPGME (2.18 Å), suggesting a stronger interaction of ethanol with the Mn center. The stabilization energy is indeed higher in the case of ethanol absorption (-53.2 kJ×mol^{-1}) than for DPGME absorption (-33.7 kJ×mol^{-1}). Note, however, that ethanol is not in dual site contact with the active slab, because of the very weak interaction with the gold cluster (Figure S9). In particular, the shortest ethanol-Au distance, 2.96 Å, is much greater than the closest DPGME-Au contact (2.35 Å). This indicates that, with respect to DPGME, ethanol interacts more strongly with Mn_3O_4, but much more weakly with the gold cluster. Overall, these interactions can be visualized by inspecting the electronic density isosurfaces of the two models (Figure 7): while there is no significant electronic density overlap between gold and ethanol, a net density overlap is clearly present in the DPGME case. Hence, the remarkably higher response and selectivity of DPGME with respect to ethanol can be explained by the interaction of DPGME with both the gold nanoparticle and the Mn_3O_4 surface.

■ CONCLUSIONS

In this work we showed that Mn_3O_4 systems functionalized with noble metal nanoparticles are endowed by remarkable capabilities for gas sensing applications. Our comprehensive theoretical and experimental characterization highlighted the occurrence of an intimate contact between Mn_3O_4 (*haussmannite*), vapor deposited on alumina substrates, and highly dispersed Ag or Au nanoparticles, introduced by sputtering under mild conditions. This feature enabled to successfully boost functional performances for the detection not only of standard volatile organic compounds (acetone and ethanol), but also of di(propyleneglycol) monomethyl ether, simulant of nitrogen mustard warfare agent, providing the best responses so far for the latter analyte. The sensing of DPGME, activated at the Mn_3O_4 interface *via* dual anchoring to both oxide and metal components, was successfully accomplished, enabling its selective discrimination from other possible CWA interferents. The active role of metal NPs in DPGME sensing accounts for the improved detection efficiency of the target nanocomposites with respect to bare Mn_3O_4, as well as for the registered outstanding responses and ultra-low detection limits.

As a whole, this study represents an important step for-

ward to highly efficient sensing devices fabricated by dual metal oxide-metal NP composites. The obtained results pave the way to mastering next generation sensing devices for real-world applications, which will be pursued by additional investigation on the system long-term stability and humidity influence on the resulting functional performances.

■ ASSOCIATED CONTENT

Supporting Information. Details on experimental procedures and theoretical calculations; further experimental data, including AFM, EDXS, XPS, and gas sensing results. This material is available free of charge via the Internet at http://pubs.acs.org.

■ AUTHOR INFORMATION

Corresponding Authors

* davide.barreca@unipd.it; chiara.maccato@unipd.it

■ ORCID

Lorenzo Bigiani: 0000-0001-7404-2340
Dario Zappa: 0000-0001-9838-7511
Davide Barreca: 0000-0002-8779-3386
Alberto Gasparotto: 0000-0003-4626-651X
Cinzia Sada: 0000-0002-7607-0481
Gloria Tabacchi: 0000-0002-1988-6775
Ettore Fois: 0000-0002-7170-8458
Elisabetta Comini: 0000-0003-2559-5197
Chiara Maccato: 0000-0001-6368-5754

Author Contributions

The manuscript was written through contributions of all authors.

Notes

The authors declare no competing financial interest.

■ ACKNOWLEDGMENT

This work was supported by Padova University DOR 2016–2019 and P-DiSC #SENSATIONAL BIRD2016-UNIPD and #03BIRD2018-UNIPD OXYGENA projects, and by University of Insubria FAR 2017-2018 project. Thanks are also due to Dr. G. Carraro for assistance and useful discussions.

■ REFERENCES

(1) Horrillo, M. C.; Martí, J.; Matatagui, D.; Santos, J. P.; Sayago, I.; Gutiérrez, J.; Martin-Fernandez, I.; Ivanov, P.; Gràcia, I.; Cané, C. Single-Walled Carbon Nanotube Microsensors for Nerve Agent Simulant Detection. *Sens. Actuators, B* **2011**, *157*, 253-259.
(2) Lee, S. C.; Kim, S. Y.; Lee, W. S.; Jung, S. Y.; Hwang, B. W.; Ragupathy, D.; Lee, D. D.; Lee, S. Y.; Kim, J. C. Effects of Textural Properties on the Response of a SnO_2-Based Gas Sensor for the Detection of Chemical Warfare Agents. *Sensors* **2011**, *11*, 6893-6904.
(3) Choi, N.-J.; Kwak, J.-H.; Lim, Y.-T.; Bahn, T.-H.; Yun, K.-Y.; Kim, J.-C.; Huh, J.-S.; Lee, D.-D. Classification of Chemical Warfare Agents using Thick Film Gas Sensor Array. *Sens. Actuators, B* **2005**, *108*, 298-304.
(4) Lee, D. D.; Choi, N. J., Metal-Oxide Based Toxic Gas Sensors. Yao, S. Z.; Tuttle, B.; Randall, C.; Viehland, D., Eds. in *Advances in Electronic Ceramic Materials*, The American Ceramic Society: 2005; Vol. *26*, pp 25-36.
(5) Lee, W. S.; Lee, S. C.; Lee, S. J.; Lee, D. D.; Huh, J. S.; Jun, H. K.; Kim, J. C. The Sensing Behavior of SnO_2-based Thick-Film Gas Sensors at a Low Concentration of Chemical Agent Simulants. *Sens. Actuators, B* **2005**, *108*, 148-153.
(6) Matatagui, D.; Martí, J.; Fernández, M. J.; Fontecha, J. L.; Gutiérrez, J.; Gràcia, I.; Cané, C.; Horrillo, M. C. Chemical Warfare Agents Simulants Detection with an Optimized SAW Sensor Array. *Sens. Actuators, B* **2011**, *154*, 199-205.
(7) Matatagui, D.; Fernández, M. J.; Fontecha, J.; Sayago, I.; Gràcia, I.; Cané, C.; Horrillo, M. C.; Santos, J. P. Characterization of an Array of Love-Wave Gas Sensors Developed using Electrospinning Technique to Deposit Nanofibers as Sensitive layers. *Talanta* **2014**, *120*, 408-412.
(8) Matatagui, D.; Fontecha, J.; Fernández, M. J.; Aleixandre, M.; Gràcia, I.; Cané, C.; Horrillo, M. C. Array of Love-Wave Sensors Based on Quartz/Novolac to Detect CWA Simulants. *Talanta* **2011**, *85*, 1442-1447.
(9) Sayago, I.; Matatagui, D.; Fernández, M. J.; Fontecha, J. L.; Jurewicz, I.; Garriga, R.; Muñoz, E. Graphene Oxide as Sensitive Layer in Love-Wave Surface Acoustic Wave Sensors for the Detection of Chemical Warfare agent Simulants. *Talanta* **2016**, *148*, 393-400.
(10) Fallis, I. A.; Griffiths, P. C.; Cosgrove, T.; Dreiss, C. A.; Govan, N.; Heenan, R. K.; Holden, I.; Jenkins, R. L.; Mitchell, S. J.; Notman, S.; Platts, J. A.; Riches, J.; Tatchell, T. Locus-Specific Microemulsion Catalysts for Sulfur Mustard (HD) Chemical Warfare Agent Decontamination. *J. Am. Chem. Soc.* **2009**, *131*, 9746-9755.
(11) Wu, H.-C.; Bayley, H. Single-Molecule Detection of Nitrogen Mustards by Covalent Reaction within a Protein Nanopore. *J. Am. Chem. Soc.* **2008**, *130*, 6813-6819.
(12) Yun, K.-H.; Yun, K.-Y.; Cha, G.-Y.; Lee, B. H.; Kim, J. C.; Lee, D.-D.; Huh, J. S. Gas Sensing Characteristics of ZnO-doped SnO_2 Sensors for Simulants of the Chemical Agents. *Mater. Sci. Forum* **2005**, *486-487*, 9-12.
(13) Zhou, X.; Zeng, Y.; Liyan, C.; Wu, X.; Yoon, J. A Fluorescent Sensor for Dual-Channel Discrimination between Phosgene and a Nerve-Gas Mimic. *Angew. Chem. Int. Ed.* **2016**, *55*, 4729-4733.
(14) Rahaman, H.; Kundu, S.; Ghosh, S. K. Size-Selective Silver-Induced Evolution of Mn_3O_4-Ag Nanocomposites for Effective Ethanol Sensing. *ChemistrySelect* **2017**, *2*, 6991-6999.
(15) Zhang, L.; Wang, G.; Yu, F.; Zhang, Y.; Ye, B.-C.; Li, Y. Facile Synthesis of Hollow $MnFe_2O_4$ Nanoboxes Based on Galvanic Replacement Reaction for Fast and Sensitive VOCs Sensor. *Sens. Actuators, B* **2018**, *258*, 589-596.
(16) Zhang, J.; Qin, Z. Y.; Zeng, D. W.; Xie, C. S. Metal-Oxide-Semiconductor Based Gas Sensors: Screening, Preparation, and Integration. *Phys. Chem. Chem. Phys.* **2017**, *19*, 6313-6329.
(17) Sberveglieri, G.; Baratto, C.; Comini, E.; Faglia, G.; Ferroni, M.; Pardo, M.; Ponzoni, A.; Vomiero, A. Semiconducting Tin Oxide Nanowires and Thin Films for Chemical Warfare Agents Detection. *Thin Solid Films* **2009**, *517*, 6156-6160.
(18) Amara, M. A.; Larbi, T.; Labidi, A.; Karyaoui, M.; Ouni, B.; Amlouk, M. Microstructural, Optical and Ethanol Sensing Properties of Sprayed Li-Doped Mn_3O_4 Thin Films. *Mater. Res. Bull.* **2016**, *75*, 217-223.
(19) Larbi, T.; Ben Said, L.; Ben Daly, A.; Ouni, B.; Labidi, A.; Amlouk, M. Ethanol Sensing Properties and Photocatalytic Degradation of Methylene Blue by Mn_3O_4, $NiMn_2O_4$ and Alloys of Ni-manganates Thin Films. *J. Alloys Compd.* **2016**, *686*, 168-175.
(20) John, N.; Thomas, P.; Divya, K. V.; Abraham, K. E. Enhanced Room Temperature Gas Sensing of Aligned Mn_3O_4 Nanorod Assemblies Functionalized by Aluminum Anodic Membranes. *Nanotechnol.* **2018**, *29*, 335503.
(21) Zhu, Y.; Zhao, Y.; Ma, J.; Cheng, X.; Xie, J.; Xu, P.; Liu, H.; Liu, H.; Zhang, H.; Wu, M.; Elzatahry, A. A.; Alghamdi, A.; Deng, Y.; Zhao, D. Mesoporous Tungsten Oxides with Crystalline Framework for Highly Sensitive and Selective Detection of Foodborne Pathogens. *J. Am. Chem. Soc.* **2017**, *139*, 10365-10373.
(22) Hwang, B. W.; Lee, S. C.; Kim, S. Y.; Jung, S. Y.; Lee, D. D.; Park, B. H.; Kim, J. H.; Son, I. S.; Kim, J. C. Sensing Behavior of a SnO_2-Based Sensor Promoted with NiO for the Detection of Di(propylene glycol) Methyl Ether. *J. Nanoelectron. Optoelectron.* **2013**, *8*, 509-513.
(23) Garcês Gonçalves, P. R.; De Abreu, H. A.; Duarte, H. A. Stability, Structural, and Electronic Properties of Hausmannite (Mn_3O_4) Surfaces and Their Interaction with Water. *J. Phys. Chem. C* **2018**, *122*, 20841-20849.
(24) Lim, J. S.; Saldana-Greco, D.; Rappe, A. M. Improved Pseudopotential Transferability for Magnetic and Electronic Properties of Binary Manganese Oxides from DFT+*U*+*J* Calculations. *Phys. Rev. B* **2016**, *94*, 165151.
(25) Ben Said, L.; Inoubli, A.; Bouricha, B.; Amlouk, M. High Zr Doping Effects on the Microstructural and Optical Properties of Mn_3O_4 Thin Films along with Ethanol Sensing. *Spectrochim. Acta, Part A* **2017**, *171*, 487-498.
(26) Bigiani, L.; Maccato, C.; Carraro, G.; Gasparotto, A.; Sada, C.; Comini, E.; Barreca, D. Tailoring Vapor-Phase Fabrication of Mn_3O_4 Nanosystems: From Synthesis to Gas-

Sensing Applications. *ACS Appl. Nano Mater.* **2018**, *1*, 2962-2970.
(27) Kim, H.-J.; Lee, J.-H. Highly Sensitive and Selective Gas Sensors using *p*-type Oxide Semiconductors: Overview. *Sens. Actuators, B* **2014**, *192*, 607-627.
(28) Zhou, T.; Liu, X.; Zhang, R.; Wang, L.; Zhang, T. Constructing Hierarchical Heterostructured Mn_3O_4/Zn_2SnO_4 Materials for Efficient Gas Sensing Reaction. *Adv. Mater. Interfaces* **2018**, *5*, 1800115.
(29) Na, C. W.; Park, S.-Y.; Chung, J.-H.; Lee, J.-H. Transformation of ZnO Nanobelts into Single-Crystalline Mn_3O_4 Nanowires. *ACS Appl. Mater. Interfaces* **2012**, *4*, 6565-6572.
(30) Acharyya, S. S.; Ghosh, S.; Sharma, S. K.; Bal, R. Fabrication of Ag Nanoparticles Supported on One-Dimensional (1D) Mn_3O_4 Spinel Nanorods for Selective Oxidation of Cyclohexane at Room Temperature. *New J. Chem.* **2016**, *40*, 3812-3820.
(31) Frydendal, R.; Seitz, L. C.; Sokaras, D.; Weng, T. C.; Nordlund, D.; Chorkendorff, I.; Stephens, I. E. L.; Jaramillo, T. F. Operando Investigation of Au-MnO_x Thin Films with Improved Activity for the Oxygen Evolution Reaction. *Electrochim. Acta* **2017**, *230*, 22-28.
(32) Fei, Z.-Y.; Sun, B.; Zhao, L.; Ji, W.-J.; Au, C.-T. Strong Morphological Effect of Mn_3O_4 Nanocrystallites on the Catalytic Activity of Mn_3O_4 and Au/Mn_3O_4 in Benzene Combustion. *Chem. Eur. J.* **2013**, *19*, 6480-6487.
(33) Carraro, G.; Gasparotto, A.; Maccato, C.; Gombac, V.; Rossi, F.; Montini, T.; Peeters, D.; Bontempi, E.; Sada, C.; Barreca, D.; Fornasiero, P. Solar H_2 Generation via Ethanol Photoreforming on e-Fe_2O_3 Nanorod Arrays Activated by Ag and Au Nanoparticles. *RSC Adv.* **2014**, *4*, 32174-32179.
(34) Simon, Q.; Barreca, D.; Gasparotto, A.; Maccato, C.; Tondello, E.; Sada, C.; Comini, E.; Devi, A.; Fischer, R. A. Ag/ZnO nanomaterials as High performance Sensors for Flammable and Toxic Gases. *Nanotechnology* **2012**, *23*, 025502.
(35) Barreca, D.; Carraro, G.; Comini, E.; Gasparotto, A.; Maccato, C.; Sada, C.; Sberveglieri, G.; Tondello, E. Novel Synthesis and Gas Sensing Performances of CuO–TiO_2 Nanocomposites Functionalized with Au Nanoparticles. *J. Phys. Chem. C* **2011**, *115*, 10510-10517.
(36) Carraro, G.; Barreca, D.; Comini, E.; Gasparotto, A.; Maccato, C.; Sada, C.; Sberveglieri, G. Controlled Synthesis and Properties of β-Fe_2O_3 Nanosystems Functionalized with Ag or Pt Nanoparticles. *CrystEngComm* **2012**, *14*, 6469-6476.
(37) Maccato, C.; Bigiani, L.; Carraro, G.; Gasparotto, A.; Sada, C.; Comini, E.; Barreca, D. Toward the Detection of Poisonous Chemicals and Warfare Agents by Functional Mn_3O_4 Nanosystems. *ACS Appl. Mater. Interfaces* **2018**, *10*, 12305-12310.
(38) Epifani, M.; Díaz, R.; Force, C.; Comini, E.; Manzanares, M.; Andreu, T.; Genç, A.; Arbiol, J.; Siciliano, P.; Faglia, G.; Morante, J. R. Surface Modification of TiO_2 Nanocrystals by WO_x Coating or Wrapping: Solvothermal Synthesis and Enhanced Surface Chemistry. *ACS Appl. Mater. Interf.* **2015**, *7*, 6898-6908.
(39) Joshi, N.; da Silva, L. F.; Jadhav, H. S.; Shimizu, F. M.; Suman, P. H.; M'Peko, J.-C.; Orlandi, M. O.; Seo, J. G.; Mastelaro, V. R.; Oliveira, O. N. Yolk-Shelled $ZnCo_2O_4$ Microspheres: Surface Properties and Gas Sensing Application. *Sens. Actuators, B* **2018**, *257*, 906-915.
(40) Liu, G.; Hall, J.; Nasiri, N.; Gengenbach, T.; Spiccia, L.; Cheah, M. H.; Tricoli, A. Scalable Synthesis of Efficient Water Oxidation Catalysts: Insights into the Activity of Flame-Made Manganese Oxide Nanocrystals. *ChemSusChem* **2015**, *8*, 4162-4171.
(41) Briggs, D.; Seah, M. P. *Practical Surface Analysis: Auger and X-ray Photoelectron Spectroscopy*, John Wiley & Sons: New York, 2nd ed. 1990.
(42) Perdew, J. P.; Burke, K.; Ernzerhof, M. Generalized Gradient Approximation Made Simple. *Phys. Rev. Lett.* **1996**, *77*, 3865-3868.
(43) Grimme, S. Semiempirical GGA-Type Density Functional Constructed with a Long-Range Dispersion Correction. *J. Comput. Chem.* **2006**, *27*, 1787-1799.
(44) Cococcioni, M.; de Gironcoli, S. Linear Response Approach to the Calculation of the Effective Interaction Parameters in the LDA + U Method. *Phys. Rev. B* **2005**, *71*, 035105.
(45) Vanderbilt, D. Soft Self-Consistent Pseudopotentials in a Generalized Eigenvalue Formalism. *Phys. Rev. B* **1990**, *41*, 7892-7895.
(46) Giannozzi, P.; Baroni, S.; Bonini, N.; Calandra, M.; Car, R.; Cavazzoni, C.; Ceresoli, D.; Chiarotti, G. L.; Cococcioni, M.; Dabo, I.; Dal Corso, A.; de Gironcoli, S.; Fabris, S.; Fratesi, G.; Gebauer, R.; Gerstmann, U.; Gougoussis, C.; Kokalj, A.; Lazzeri, M.; Martin-Samos, L.; Marzari, N.; Mauri, F.; Mazzarello, R.; Paolini, S.; Pasquarello, A.; Paulatto, L.; Sbraccia, C.; Scandolo, S.; Sclauzero, G.; Seitsonen, A. P.; Smogunov, A.; Umari, P.; Wentzcovitch, R. M. QUANTUM ESPRESSO: A Modular and Open-Source Software Project for Quantum Simulations of Materials. *J. Phys.: Condens. Matter* **2009**, *21*, 395502.
(47) Pattern N° 024-0734, JCPDS (2000).
(48) Qiu, J.; Wu, Y.-C.; Wang, Y.-C.; Engelhard, M. H.; McElwee-White, L.; Wei, W. D. Surface Plasmon Mediated Chemical Solution Deposition of Gold Nanoparticles on a Nanostructured Silver Surface at Room Temperature. *J. Am. Chem. Soc.* **2013**, *135*, 38-41.
(49) Fu, X.-P.; Guo, L.-W.; Wang, W.-W.; Ma, C.; Jia, C.-J.; Wu, K.; Si, R.; Sun, L.-D.; Yan, C.-H. Direct Identification of Active Surface Species for the Water–Gas Shift Reaction on a Gold–Ceria Catalyst. *J. Am. Chem. Soc.* **2019**, *141*, 4613-4623.
(50) Chew, C.; Bishop, P.; Salcianu, C.; Carmalt, C. J.; Parkin, I. P. Aerosol-Assisted Deposition of Gold Nanoparticle-Tin Dioxide Composite Films. *RSC Adv.* **2014**, *4*, 13182-13190.
(51) Liu, J. J.; Liu, J. Z.; Song, W. W.; Wang, F.; Song, Y. The Role of Electronic Interaction in the Use of Ag and Mn_3O_4 Hybrid Nanocrystals Covalently Coupled with Carbon as Advanced Oxygen Reduction Electrocatalysts. *J. Mater. Chem. A* **2014**, *2*, 17477-17488.
(52) Barreca, D.; Bigiani, L.; Monai, M.; Carraro, G.; Gasparotto, A.; Sada, C.; Martí-Sanchez, S.; Grau-Carbonell,

A.; Arbiol, J.; Maccato, C.; Fornasiero, P. Supported Mn_3O_4 Nanosystems for Hydrogen Production through Ethanol Photoreforming. *Langmuir* **2018**, *34*, 4568-4574.
(53) Bigiani, L.; Barreca, D.; Gasparotto, A.; Sada, C.; Martí-Sanchez, S.; Arbiol, J.; Maccato, C. Controllable Vapor Phase Fabrication of F:Mn_3O_4 Thin Films Functionalized with Ag and TiO_2. *CrystEngComm* **2018**, *20*, 3016-3024.
(54) Bigiani, L.; Barreca, D.; Gasparotto, A.; Maccato, C. Mn_3O_4 Thin Films Functionalized with Ag, Au, and TiO_2 Analyzed using X-ray Photoelectron Spectroscopy. *Surf. Sci. Spectra* **2018**, *25*, 014003.
(55) Moulder, J. F.; Stickle, W. F.; Sobol, P. E.; Bomben, K. D. *Handbook of X-ray Photoelectron Spectroscopy*, Perkin Elmer Corporation, Eden Prairie, MN, USA 1992.
(56) http://srdata.nist.gov/xps.
(57) Deng, S.; Tjoa, V.; Fan, H. M.; Tan, H. R.; Sayle, D. C.; Olivo, M.; Mhaisalkar, S.; Wei, J.; Sow, C. H. Reduced Graphene Oxide Conjugated Cu_2O Nanowire Mesocrystals for High-Performance NO_2 Gas Sensor. *J. Am. Chem. Soc.* **2012**, *134*, 4905-4917.
(58) Catto, A. C.; Silva, L. F. d.; Bernardi, M. I. B.; Bernardini, S.; Aguir, K.; Longo, E.; Mastelaro, V. R. Local Structure and Surface Properties of $Co_xZn_{1-x}O$ Thin Films for Ozone Gas Sensing. *ACS Appl. Mater. Interf.* **2016**, *8*, 26066-26072.
(59) https://www.grainger.com/content/qt-exposure-limits-air-contam-232. https://www.grainger.com/content/qt-exposure-limits-air-contam-232.

ACS Appl. Mater. Interfaces **2019**, *11*, 23692-23700
https://doi.org/10.1021/acsami.9b04875

TOC